Intersubband Transitions in Lead Halide Perovskite-Based Quantum Wells for Mid-Infrared Detectors

*Xinxin Li[1,2], Wanyi Nie[3], Xuedan Ma[1,2,4]**

[1]Center for Nanoscale Materials, Argonne National Laboratory, Lemont, Illinois 60439, United States

[2]Consortium for Advanced Science and Engineering, University of Chicago, Chicago, Illinois 60637, United States

[3]Center for Integrated Nanotechnologies, Los Alamos National Laboratory, Los Alamos, New Mexico 87545, United States

[4]Center for Molecular Quantum Transduction, Northwestern University, Evanston, IL, 60208, USA

ABSTRACT

Due to their excellent optical and electrical properties as well as versatile growth and fabrication processes, lead halide perovskites have been widely considered as promising candidates for green energy and opto-electronic related applications. Here, we investigate their potential applications

at infrared wavelengths by modeling the intersubband transitions in perovskite-based quantum well systems. Both single-well and double-well structures are studied and their energy levels as well as the corresponding wavefunctions and intersubband transition energies are calculated by solving the one-dimensional Schrödinger equations. By adjusting the quantum well and barrier thicknesses, the intersubband transition energies can be tuned to cover a broad infrared wavelength range. We also find that the lead-halide perovskite-based quantum wells possess high absorption coefficients. The widely tunable transition energies and high absorption coefficients of the perovskite-based quantum well systems, combined with their unique material and electrical properties, may enable an alternative material system for infrared photodetector applications.

TOC

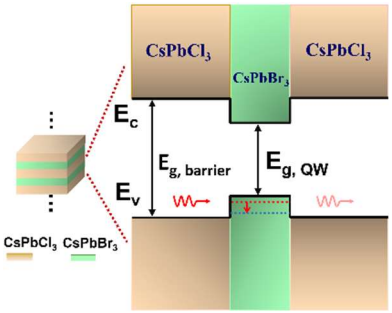

KEYWORDS: Lead halide perovskite, quantum well, intersubband transition, thermal infrared, photodetector

Spectroscopy in the thermal infrared (IR) region spanning the wavelength range of 3 – 15 μm is critical for many applications ranging from astronomy to security to environmental analysis. Detection of IR radiation could be implemented based on thermal effects like those in bolometers [(1)] or interband transitions in narrow gap ternary alloys such as mercury cadmium telluride.[(2)] An alternative approach to these technologies replies on the intersubband (ISB) transitions in epitaxially grown nanostructures such as quantum wells (QWs) and quantum dots (QDs).[(3-6)] The versatility in the compositions and electronic structures of these nanostructures allows precise tuning in their ISB transition energies and rates through the quantum confinement effect. So far, IR light sources and detectors such as quantum cascade lasers and detectors based on ISB transitions in quantum wells and quantum dots have been successfully demonstrated and utilized in many important applications.

Despite these developments in thermal IR devices based on epitaxially grown nanostructures, they remain technologically demanding and mostly limited to defense and scientific applications. Low-cost alternatives combining inexpensive material synthesis and ease of processing is highly desirable[(7)] and could potentially offer practical solutions to sophisticated device designs and their wider applications. In this regard, perovskite materials may serve as a cost-effective alternative. Specifically, their tunable compositions and versatile growth and fabrication procedures may allow the integration of multi-spectral components in a single device. Although the current generation of perovskite materials have exhibited moderate mobilities at room temperature when compared to some of the best performing inorganic semiconductors such as GaAs, their long diffusion lengths and charge recombination lifetimes ensure excellent charge extraction performance.[(8)] Moreover, perovskite materials possess benign defect properties where deep defect formation is energetically unfavorable,[(9)] indicating that high quality devices based on perovskites can be fabricated with

high tolerance to imperfections.[10] This is in stark contrast to common QW materials such as GaAs, which typically require high purity and crystallinity to obtain high device performance. Given the encouraging progresses in perovskite material design and growth, it is expected that higher carrier mobilities would be achieved in perovskites incorporating light metals.[11] These properties together position perovskites as a potentially compelling material system for developing IR devices.

Aside from these appealing material properties of perovskites, recent developments in their thin film growth and controlled doping may further facilitate their applications in IR devices. Ultrathin perovskite films that are a few nanometers thick have been grown using various approaches[12-14] and interband emission from such perovskite-based QWs has been demonstrated.[12] Although efficient and reliable tuning of carrier densities in perovskites has been proved to be challenging, encouraging progresses have been achieved through chemical composition and crystal structure engineering.[15, 16] These developments provide necessary foundations for the implementation of IR devices based on perovskites.

Here, we theoretically explore QW structures based on perovskite materials that would allow ISB transitions suitable for IR applications. Using cesium lead halide perovskites ($CsPbX_3$) as an illustrative case, we start by investigating the energy levels and ISB transitions in perovskite-based single quantum wells (SQWs) and then continue on to symmetric double quantum wells (DQWs). ISB transitions corresponding to IR wavelengths are achieved by tuning the well and barrier thicknesses. We demonstrate that large ISB absorption coefficients can be achieved in the 5 – 11 μm wavelength range in $CsPbX_3$-based SQWs and DQWs, making them promising materials for IR photodetectors.

Although previous studies have reported the coexistence of orthorhombic and cubic phases in nanocrystalline $CsPbBr_3$ at room temperature,[17, 18] during our simulation, we consider a simplified situation and assume the crystal structure to be cubic, as illustrated in Figure 1. Cubic ABX_3 perovskites have direct bandgaps at the R point (½, ½, ½) of the Brillouin zone.[19]

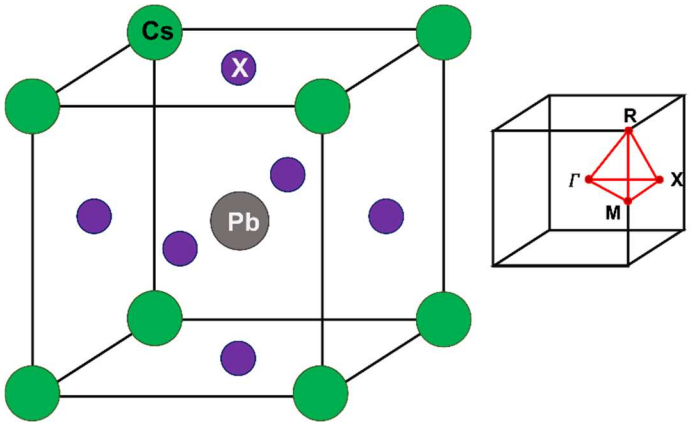

Figure 1. Crystalline structures of cubic $CsPbX_3$ perovskites. The inset is an illustration of the Brillouin zone of the cubic structure.

Figure 2(a) shows the representative band structure of cubic $CsPbX_3$ perovskites. The top of their valence band (blue curve in Figure 2(a)) is *s*-like which is doubly degenerated considering the spin degeneracy. Due to the strong spin-orbit coupling (SOC) in $CsPbX_3$ perovskites, the well-known Pb 6*p* orbitals convert to a singlet state at the bottom of conduction band (pink curve in Figure 2(a)) and a three-fold degenerated triplet state with the degeneracy multiplying by 2 considering spin.[19] The top two conduction bands in Figure 2(a) represent the light electron (LE) and heavy electron (HE) states, respectively, while the bottom of the conduction band is the split-off (SO) state with a spin-split off energy $\Delta_{SO} = 1.5$ eV for $CsPbBr_3$.[20] This is in stark contrast to the band structures observed in common III-V semiconductors (Figure 2(b)) which consist of a *s*-like

conduction band and a valence band comprised of a heavy hole (HH), a light hole (LH) and a SO state. In the following discussions, we deliberately invert the band structures of the perovskite-based QWs in the y-direction to make direct comparison to conventional III-V systems as demonstrated in Figure 2(b) more straightforward.

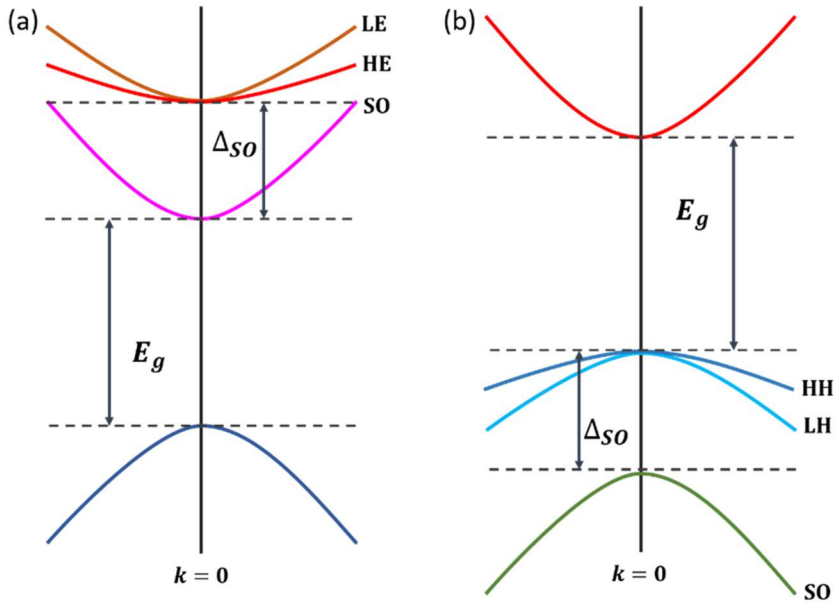

Figure 2. Band edge energy levels in (a) $CsPbX_3$ perovskites and (b) III-V semiconductors.

The eigenvectors of the effective mass tensor are oriented along the Pb-Pb directions which are all equivalent for cubic structure.[21] We assume both the hole and electron masses to be isotropic in our simulation. Table 1 lists the major parameters, including the lattice constants, band gaps (E_g), effective masses, Luttinger parameters, dielectric constants, and phonon energies of the $CsPbX_3$ materials used in this study. Solution-grown $CsPbX_3$ perovskites normally show slightly *p*-type behavior[22] with hole concentrations less than 10^{14} cm^{-3}.[23] Given such low doping concentrations, we assume the as-grown $CsPbX_3$ perovskites to be undoped in our calculations unless otherwise mentioned.

Table 1. Parameters used for the calculations of the energy band diagrams and wavefunctions.

Parameters	$CsPbBr_3$	$CsPbCl_3$
Lattice constant (Å) [24, 25]	5.77	5.62
E_g (eV) [20, 25]	2.34	3.04
$m_h(m_0)$ [20, 26]	0.26	0.17
$m_{he}(m_0)$ [20]	1.605	1.619
$m_{le}(m_0)$ [20]	0.303	0.357
$m_{SO}(m_0)$ [20]	0.509	0.584
Δ_{SO} (eV) [19]	1.5	1.54
γ_1^L [20]	7.6	5.8
γ_2^L [20]	3.0	2.2
γ_3^L [20]	0.7	0.5
Static dielectric constant ε_s [27]	15.6	15.6
High frequency dielectric constant ε_∞ [27, 28]	4.96	4.5
LO phonon Energy (meV) [29-31]	18	42.8

We first consider SQW structures based on $CsPbX_3$ perovskites. Lee *et al* have recently reported experimental results of interband transitions at visible wavelengths from $CsPbBr_3$-based SQWs with 1,3,5-tris(N-phenylbenzimidazol-2-yl)benzene (TPBi) as the barriers: By alternatively depositing TPBi and $CsPbBr_3$ thin films onto glass substrates, $CsPbBr_3$/TPBi quantum wells were obtained and characterized. To benchmark our simulation, we start by calculating the interband

transitions in a similar SQW structure and comparing our simulation results to the reported experimental values. The valence and conduction band offset energies are set to be 0.53 eV and 0.32 eV, respectively, which are derived from the band alignment between $CsPbBr_3$ and TPBi. [12] The width of the $CsPbBr_3$ SQW is varied from 2 to 20 nm while that of the TPBi barrier is fixed to be 7 nm.

Figure 3(a) shows the simulated wavefunctions and energy levels of a representative 5 nm thick $CsPbBr_3$ SQW embedded in TPBi barriers. From top to down, the bands are the valence band E_V and conduction band E_C, respectively. Due to the large band offsets between the QW and the barriers, both the electrons and holes are highly confined in the QW region. A reasonable agreement between the bandgaps obtained from our simulations and those derived from the experimental data in Ref. (12) can be observed (Figure 3(b)). For the QWs with thicknesses smaller than the Bohr radius of $CsPbBr_3$ (~ 7 nm),[32] a prominent quantum confinement effect is expected, as is evident from Figure 3(b). The bandgap increases from around 2.4 eV for a 10 nm thick SQW to ~2.6 eV for a 2 nm thick SQW, a trend that can be well described by the simple "particle-in-a-box" model which assumes that the interband transition energy is inversely proportional to the carrier effective mass (Figure 3(b), cyan curve).[12] These simulation results attest the accuracy of the eight-band $\boldsymbol{k} \cdot \boldsymbol{p}$ approach (see the Methods section for details), which we will apply primarily in our following calculations of the intersubband transitions in the perovskite quantum well structures.

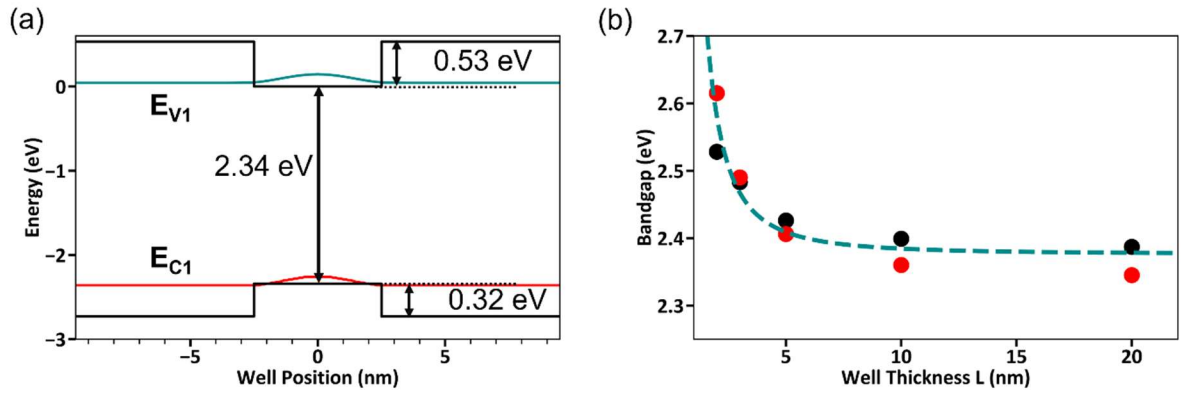

Figure 3. (a) Band alignment and wavefunctions of a 5 nm thick single $CsPbBr_3$ quantum well surrounded by 7 nm thick TPBi barriers. E_{V1} and E_{C1} are the lowest energy levels in the valence and conduction bands, respectively. Note that the band structures plotted here are inverted in the y-direction to mimic the case of conventional III-V QW systems. (b) Calculated bandgap energies of $CsPbBr_3$/TPBi single quantum well/barrier structures with varying well thicknesses (red dots) compared to those derived from the experimental data in Ref. (12) (black dots). The cyan curve is a fit of the data using the "particle-in-a-box" model.

To investigate the ISB transitions in perovskite QWs, we use the widely studied $CsPbBr_3$ as the quantum well material for illustrative purposes, although we expect similar design principles can be applied to other perovskite systems. For simplicity, $CsPbCl_3$ is employed as the barrier due to their large band offsets with respect to $CsPbBr_3$ and widely available material parameters. $CsPbCl_3$ also has a large carrier mobility[33] (orders of magnitude higher than that of TPBi),[34] which could greatly benefit device performance for practical applications. Same as in the case of the QW materials, in practice $CsPbCl_3$ can be replaced by other materials as long as they meet the band alignment requirements to serve as the barriers. We assume alternative growth/deposition of

$CsPbCl_3$ and $CsPbBr_3$ thin films of designated thicknesses could lead to the proposed QW/barrier heterostructures.

In the proposed $CsPbBr_3/CsPbCl_3$ QW/barrier heterostructure, due to the non-negligible 2.5% lattice mismatch between $CsPbBr_3$ and $CsPbCl_3$, we estimate the critical thickness for $CsPbBr_3$ to grow on $CsPbCl_3$ with dislocation free transition to be around 9 nm[35] by assuming a Poisson's ratio of around 0.28.[36] Therefore, in our simulations, the thickness of the $CsPbBr_3$ SQW is kept below the critical thickness, while the $CsPbCl_3$ barrier thickness is fixed to 10 nm. The absolute conduction and valence band edge energy levels were reported to be -3.26 eV and -6.24 eV for $CsPbCl_3$,[37] and -3.6 eV and -5.9 eV for $CsPbBr_3$,[38] which give rise to around the same conduction and valence offsets of 0.34 eV.

Figure 4(a) depicts the band structure of a representative 5 nm thick $CsPbBr_3$ SQW sandwiched between two 10 nm $CsPbCl_3$ barrier layers. From top to down, the bands correspond to the valence, SO and HE/LE states, respectively. Figure 4(b) shows wavefunctions of the three lowest states, namely the ground state $|1\rangle$, the first and the second excited states $|2\rangle$ and $|3\rangle$, that are confined in the valence band of the 5 nm thick SQW. Much like in III-V QWs, the ISB transitions in the perovskite QWs are only allowed between states with same parity. The ISB transitions that are allowed by the optical selection rules have energies of $E_{32} = E_3 - E_2 = 120.6\,\text{meV}$ and $E_{21} = E_2 - E_1 = 85.4\,\text{meV}$, respectively. We obtained corresponding ISB transition dipole moments of $\boldsymbol{z_{32}} = 1.35\,\text{nm}$ and $\boldsymbol{z_{21}} = 1.21\,\text{nm}$, respectively, which are comparable to those commonly obtainable in III-V QWs.[39]

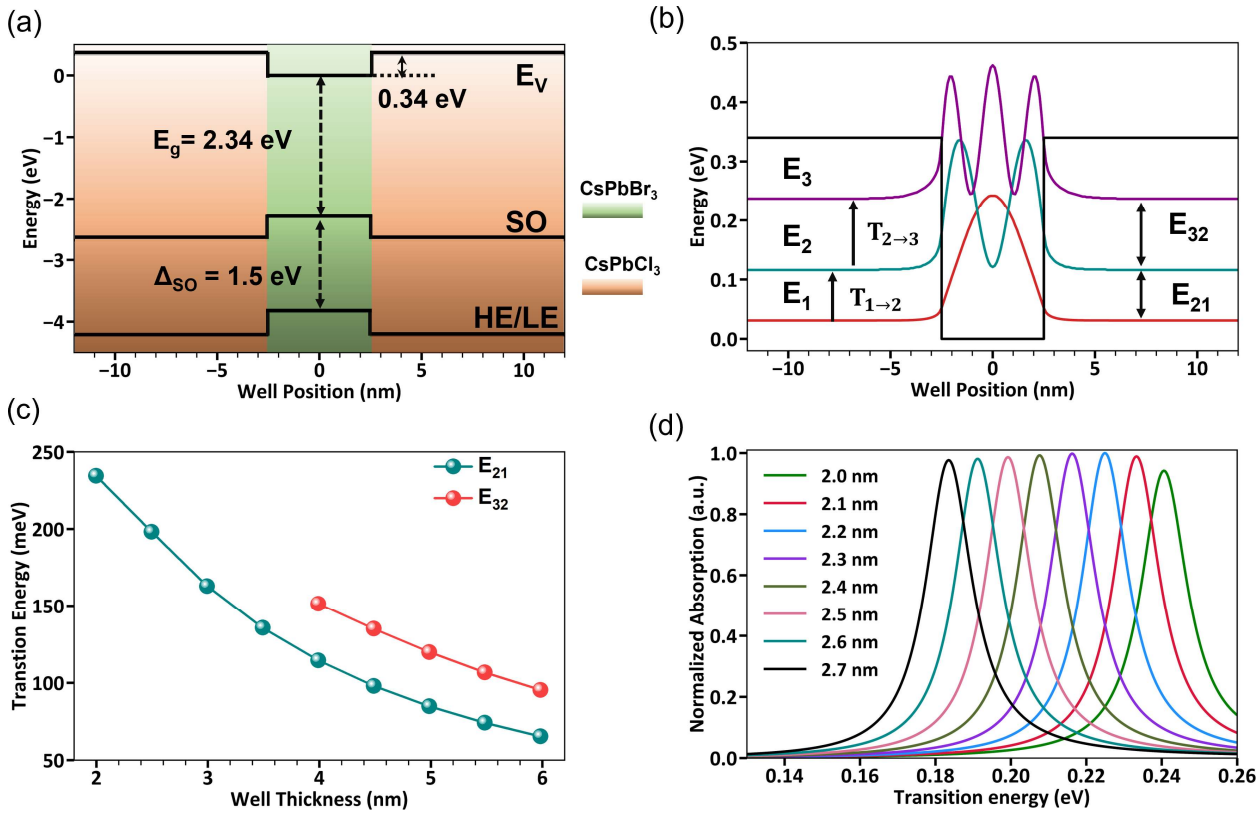

Figure 4. (a) Schematic illustration of the energy bands in a 5 nm thick SQW. (b) Wavefunctions of the three confined states in the valence band. (c) Transition energy E_{32} and E_{21} versus well thickness. (d) Absorption coefficient for $T_{1->2}$ transitions in SQW structures with varying well thicknesses at the same doping level of 5×10^{17} cm^{-3} normalized to the maximum achievable value (~ 660 cm^{-1} occurring at a well thickness of 2.2 nm, blue curve). Note the band structures plotted in (a) and (b) are inverted in the y-direction.

One of the major advantages offered by ISB transitions is their flexibility in tailoring the transition energies through tuning the quantum well thickness. We systematically investigate the influence of the quantum well thickness on the ISB transition energies and the simulation obtained results are shown in Figure 4(c). When the quantum well becomes thinner, ISB transition energies E_{32}

and E_{21} increase accordingly. Changes in the SQW thickness also affect the electronic states that can be confined in the SQWs. When the SQW is thinner than 4.0 nm, energy level of the second excited state $|3\rangle$ becomes higher than that of the barrier. Consequently, only the ground state $|1\rangle$ and the first excited state $|2\rangle$ can be confined in the SQWs (see Figure S1 for an example) and only E_{21} can be obtained (Figure 4(c)). In contrast, when the SQW is thicker than 5.5 nm, energy level of the third excited state E_4 becomes lower than the barrier height and it becomes confined in the SQW. By adjusting the SQW thickness, we are able to tune the ISB transition energies from 235 meV to 66 meV, covering most of the thermal IR range. We would like to note that although our discussions have focused on the exemplary case of $CsPbBr_3/CsPbCl_3$ QW/barrier system, tuning barrier heights by adjusting the system's compositions could be another viable approach to achieve control over the ISB transition energies. In addition, the large variety of perovskite materials with diverse energy levels[40] could further allow the tuning of barrier heights in a wide range of values.

Figure 4(d) illustrates the normalized absorption coefficient for intersubband transition $T_{1->2}$ in SQWs with well thickness varying from 2.0 to 2.7 nm. To bring the Fermi level above E_1, we deliberately *p*-dope the central region of the SQW with a symmetric doping profile. The doped region is fixed to be 9 nm regardless of the well thickness in order to keep the doping profile consistent. A high doping level could lead to band bending, as illustrated in Figure S1. Since the absorption coefficient is also highly dependent on the doping concentration,[41] we assume the same doping level of 5×10^{17} cm^{-3} for all the SQWs. We note that the doping level we adapt here for the simulations is already achievable experimentally,[42, 43] although more studies are required for better controllability. In Figure 4(d), it is noticeable that the absorption coefficient first increases with the reducing well thickness and then decreases, which is consistent with previous

reports on III-V SQWs.[44] The maximum absorption coefficient (~ 660 cm^{-1} with a doping concentration of 5×10^{17} cm^{-3}) occurs at the well thickness of around 2.2 nm (Figure 4(d), blue curve), which corresponds to an E_{21} value of around 226 meV. This implies that an optimal absorption efficiency of ISB transition photodetectors based on $CsPbBr_3$ SQWs is likely to occur at a working wavelength of around 5.5 μm. We also investigate the influence of the doping level, and observe that the maximum achievable absorption coefficient of the SQWs increases consistently with the doping level accompanied by a reduction in the transition energy (Supporting information Figure S2). Moreover, aside from the tunable operation wavelength spanning 5 - 7 μm, the simulation obtained nominal absorption coefficients of the studied SQWs are relatively high, comparable to those of GaAs SQW (~ 1400 cm^{-1} for a 2.2×10^{17} cm^{-3} doping level).[45] From Eq. 11 and 12, we derive that the relatively smaller refractive indices of perovskite materials compared to those of III-V semiconductors could be beneficial for obtaining larger ISB absorption coefficients. These large ISB absorption coefficients, combined with the long charge carrier diffusion lengths and defect tolerant properties of the perovskite materials, may potentially offer an alternative material system for high performance ISB transition photodetectors.

Compared to SQWs, multiple-well structures provide wider energy tunability due to the possibility to separate the charge carriers in the different QWs by manipulating the well and barrier thicknesses. Figure 5(a) shows a representative symmetric DQW structure comprised of two identical $CsPbBr_3$ quantum wells both with a well thickness of 2.5 nm and a central $CsPbCl_3$ barrier with a thickness of 1.5 nm. The thicknesses of the side barriers are fixed to be 7 nm. Figure 5(b) illustrates the four energy levels confined in the symmetric DQW. Our numerical calculations yield ISB transition energies of $E_{41} = 231.9$ meV, $E_{32} = 178.2$ meV and $E_{21} = 17.2$ meV, with the latter being close to the longitudinal optical phonon energies in $CsPbBr_3$ (around 18 meV).[46] To

investigate the influence of the central barrier thickness, we keep the thickness of both QWs to 2.5 nm and adjust the barrier thickness from 1.0 nm to 2.0 nm. As can be seen in Figure 5(c), an increase in the central barrier thickness reduces E_{21} but increases E_{32}. On the other hand, if we keep the central barrier thickness at 1.0 nm and tune the thickness of the QWs, both E_{32} and E_{21} decrease with the increasing well thickness (Figure 5(d)). These simulation results reveal the flexibility in tuning the transition energies in the DQWs. The functionality of the DQWs can be further extended if asymmetric quantum wells are considered.

We further consider the potential of using the ISB transitions in perovskite coupled QWs (CQWs) for photodetection applications by simulating the achievable absorption coefficients in these heterostructures. Since energy levels $|1\rangle$ and $|2\rangle$ are close in the current design, transitions that are of interest for mid-IR application is from energy level $|1\rangle$ to $|4\rangle$ denoted as $T_{1->4}$ or $|2\rangle$ to $|3\rangle$ denoted as $T_{2->3}$. We again *p*-dope 9 nm of the central region to 5×10^{17} cm^{-3}. In this case, the Fermi level is raised to above energy level $|1\rangle$ but below $|2\rangle$. We first investigate the influence of the central barrier thickness on the absorption coefficient by keeping the quantum well thickness fixed at 2.1 nm while tuning the central barrier thickness from 2.2 to 3.8 nm. As can be seen in Figure 5(e), the absorption coefficient for the $T_{1->4}$ transition first increases with the central barrier thickness and then decrease with a maximum (500 cm^{-1}) occurring at the central barrier thickness of 2.8 nm, to which all the absorption coefficients in Fig. 5(e) are normalized. As the barrier gets thicker, energy level $|2\rangle$ shifts to below the Fermi level, making the $T_{2->3}$ transition achievable. We also investigate the influence of quantum well thickness on the absorption coefficient. By keeping the central barrier thickness to 2.8 nm, the absorption coefficient maximum of around 504 cm^{-1} is found for a quantum well thickness of 2.2 nm (Figure 5(f)). To investigate $T_{2->3}$ transition in the CQWs, we increase the *p*-doping level to 3×10^{18} cm^{-3} to bring the Fermi level to above

energy level $|2\rangle$. The absorption coefficient associated with the $T_{2->3}$ transition in Figure 5(g) and (h) shows similar trends as in Figure 5(e) for varying central barrier thickness and in Figure 5(f) for various well thicknesses. The maximum absorption coefficient of 1757 cm^{-1} occurs at a central barrier of 1.5 nm and well thickness of 2.2 nm (Figure 5(g) and (h)). Our simulations of CQWs with various doping concentrations suggest that influence of the doping concentration on the absorption coefficient is similar to that in the SQWs: an increase in the doping level leads to a larger maximum achievable absorption coefficient (Figure S2(b) and (c)). At a doping level of 1×10^{18} cm^{-3}, the absorption coefficient due to $T_{1->4}$ transition can be as large as 880 cm^{-1} (Figure S2(b)) with an optimal working wavelength of ~ 5.1 μm ($E_{41} = 241$ meV). Doping dependent absorption coefficient of $T_{2->3}$ is also investigated (Figure S2(c)), although some of the doping levels could be challenging to achieve experimentally. We note that although absorption coefficients of the $T_{1->4}$ and $T_{2->3}$ transitions in the DQWs are comparable to the $T_{1->2}$ transition in the SQW systems discussed in the previous section with similar doping profiles, the DQW geometries studied in Figure 5(e) - 5(h) provide high absorption coefficients covering a much wider working wavelength range (from around 5 to 11 μm).

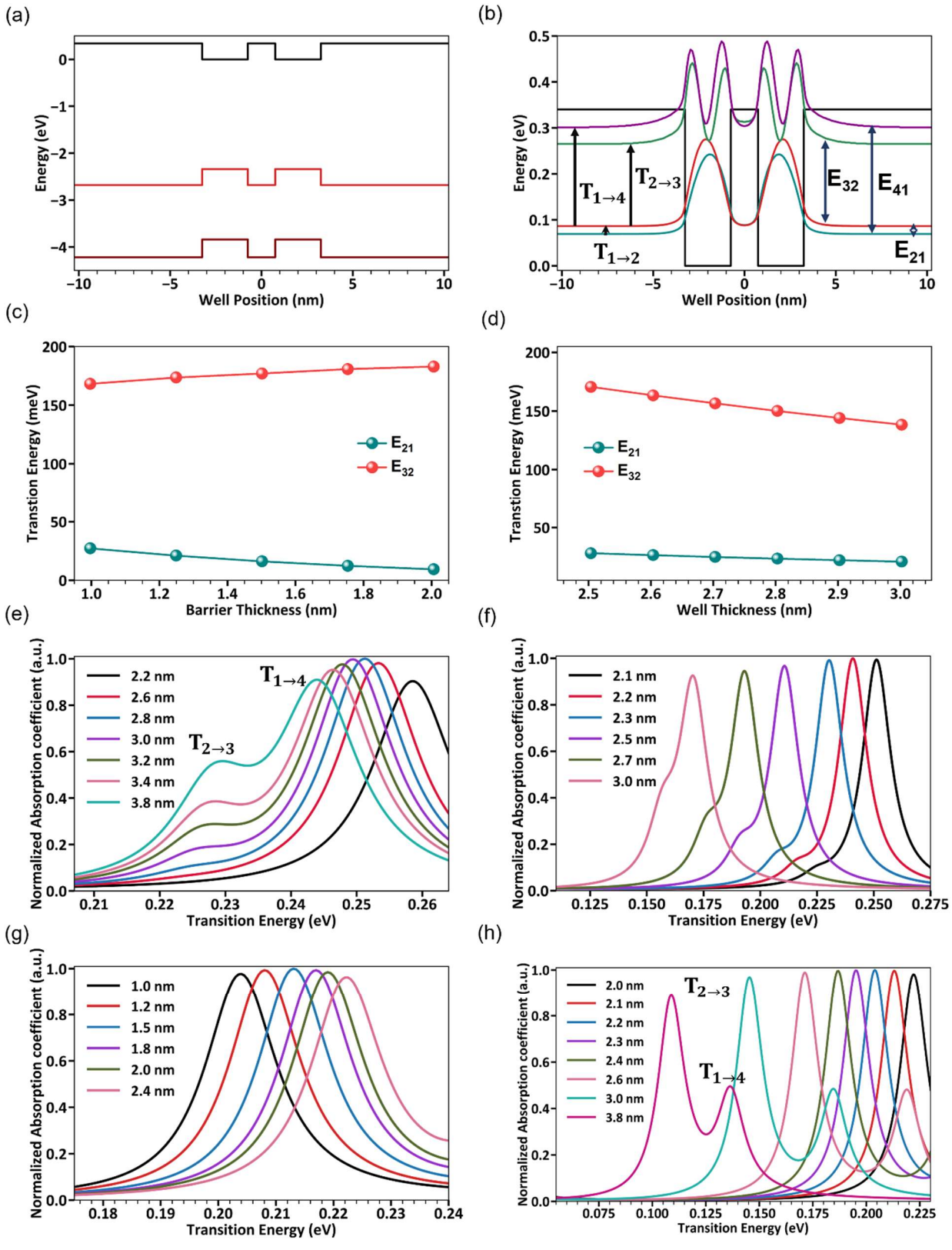
(a)
Energy (eV)
Well Position (nm)
(b)
Energy (eV)
$T_{1\to4}$
$T_{2\to3}$
$T_{1\to2}$
E_{32}
E_{41}
E_{21}
Well Position (nm)
(c)
Transtion Energy (meV)
E_{21}
E_{32}
Barrier Thickness (nm)
(d)
Transtion Energy (meV)
E_{21}
E_{32}
Well Thickness (nm)
(e)
Normalized Absorption coefficient (a.u.)
2.2 nm
2.6 nm
2.8 nm
3.0 nm
3.2 nm
3.4 nm
3.8 nm
$T_{1\to4}$
$T_{2\to3}$
Transition Energy (eV)
(f)
Normalized Absorption coefficient (a.u.)
2.1 nm
2.2 nm
2.3 nm
2.5 nm
2.7 nm
3.0 nm
Transition Energy (eV)
(g)
Normalized Absorption coefficient (a.u.)
1.0 nm
1.2 nm
1.5 nm
1.8 nm
2.0 nm
2.4 nm
Transition Energy (eV)
(h)
Normalized Absorption coefficient (a.u.)
2.0 nm
2.1 nm
2.2 nm
2.3 nm
2.4 nm
2.6 nm
3.0 nm
3.8 nm
$T_{2\to3}$
$T_{1\to4}$
Transition Energy (eV)

Figure 5. (a) Schematic of the energy levels in a $CsPbBr_3/CsPbCl_3$ symmetric DQW. (b) Wavefunctions of the confined states in the valence band of a 2.5 nm/1.5 nm/2.5 nm DQW obtained from the $\boldsymbol{k \cdot p}$ method. (c) Central barrier thickness-dependent transition energies, E_{21} and E_{32} of the DQWs. (d) Quantum well thickness-dependent transition energies, E_{21} and E_{32}. (e, f) Normalized absorption coefficient of $CsPbBr_3/CsPbCl_3$ symmetric DQWs at a doping level of 5×10^{17} cm^{-3} with (e) central barrier thickness varying from 2.2 to 3.8 nm and a fixed well thickness of 2.1 nm, and (f) well thickness varying from 2.1 to 3.0 nm and a fixed central barrier of 2.8 nm. Absorption coefficients in (e) are normalized to a maximum value of 500 cm^{-1} corresponding to a central barrier thickness of 2.8 nm (blue curve in (g)), and those in (f) are normalized to a maximum value of 504 cm^{-1} occurring at a quantum well thickness of 2.2 nm (red curve in (f)). (g, h) Normalized absorption coefficient of the symmetric DQWs doped to 3×10^{18} cm^{-3} with (g) central barrier thickness varying from 1.0 to 2.4 nm and fixed well thickness of 2.1 nm, and (h) well thickness varying from 2.0 to 3.8 nm with a fixed central barrier of 1.5 nm thick. The low energy peaks correspond to $T_{2->3}$ transitions and the higher energy peaks correspond to $T_{1->4}$ transitions. Absorption coefficients in (g) are normalized to the maximum absorption coefficient (1757 cm^{-1}) of a 2.1 nm/1.5 nm $CsPbBr_3/CsPbCl_3$ symmetric DQW (blue curve in (g)), and those in (h) are normalized to the maximum absorption coefficient (1757 cm^{-1}) of a 2.2 nm/1.5 nm symmetric DQW (blue curve in (h)). Note the band structures plotted in (a) and (b) are inverted in the y-direction.

Moreover, DQWs could allow decoupling of the ground and excited states in the different QWs, thus afford more tunability both in terms of the covered ISB transition energies and rates. This is of particular importance when designing ISB transitions in QWs for IR light source applications.

In these cases, a three-level system is typically used with level $|1\rangle$ being the ground state and $|2\rangle$ and $|3\rangle$ the first and second excited states. When electrons are optically excited or electrically injected into the second excited level, population inversion and simulated emission occur between the first $|2\rangle$ and second $|3\rangle$ excited states provided that the lifetime of the first excited level $|2\rangle$ is shorter than that of the second excited level $|3\rangle$, which can be achieved by tuning the energy spacing between the subbands to promote or inhibit relevant electron-phonon interactions.[39] Specifically, the optical gain in such a three-level system is determined by:[47] $F \propto (1 - \tau_{21}/\tau_{32}) \cdot \tau_3 \cdot z_{31}^2 z_{32}^2$, where τ_{21} and τ_{32} are the ISB transition lifetimes, $\tau_3 = ({\tau_{31}}^{-1} + {\tau_{32}}^{-1})^{-1}$ is the lifetime at the second excited state $|3\rangle$, and z_{31} and z_{32} are the ISB transition dipole matrix elements. In our scattering lifetime calculations, we mainly consider the predominant carrier-LO phonon scattering mechanism (see Supporting Information S3 for details). The scattering lifetime, τ_{if}, from an initial state *i* to a final state *f* is highly dependent on the carrier-phonon interaction overlapping integral, where the integration covers the allowed values of optical phonon wave vector. In order to have the first excited state relax much faster than the second excited state to achieve population inversion, *i.e.* $\tau_{21} \ll \tau_{32}$, the first excited state could be chosen to be spaced by the optical phonon energy from the ground state to promote carrier-phonon interaction. In the example case shown in Figure 5(a) and 5(b), the E_{21} transition energy is tuned to be close to the longitudinal optical phonon energies in $CsPbBr_3$. Therefore, this DQW profile may allow the efficient depopulation of the first excited level $|2\rangle$ and facilitate population inversion between the second and first excited states, thus offering optical gains unattainable using SQWs (see Supporting Information S3 for details). We note that while this design principle has been implemented successfully in III-V QWs, the abundance of different phonon modes in perovskites caused by either the motions of the inorganic lead halide ions or the lattice vibrations of the organic

cations signify the importance of suppressing carrier-phonon interactions in order to obtain high gains in perovskite-based IR photon sources. Recent experimental demonstrations show that the application of inorganic perovskites incorporating light metals can effectively eliminate phonon modes associated with the organic cations and increase the phonon frequencies.[8] The versatile compositions of the perovskite materials may offer promising controls over the gain properties of perovskite-based IR photon sources.

In summary, we construct $CsPbBr_3/CsPbCl_3$ SQWs and symmetric DQW structures with varying well and barrier thicknesses and calculate their wavefunctions, intersubband transition energies and absorption coefficients. Our simulations show that highly *p*-doped SQWs with a 2.2 nm well thickness provides maximum achievable absorption coefficients (~ 660 cm^{-1} at the doping concentration of 5×10^{17} cm^{-3}) at a working wavelength of ~ 5.5 μm. The DQWs demonstrate similar absorption coefficients as the SQWs, but they can cover a broader working wavelength range by tuning the well and barrier thicknesses. Because the DQWs could allow decoupling of the ground and excited states in the different QWs, they afford larger gain coefficients compared to the SQWs and potentially are suitable for IR photon sources. The widely tunable transition energies and large absorption coefficients of the lead halide perovskites-based quantum well structures make them promising alternative candidates for IR applications.

Methods

Theoretical Calculation Details

We use cesium lead halides ($CsPbX_3$) as the prototype perovskite materials for the design of QWs for IR applications. We expect similar approaches and conclusions can be extended to other types of inorganic perovskite materials. One-dimensional (1D) Schrödinger equations were solved numerically using the software package *nextnano*^{3}.[48] Due to the relatively large bandgaps of the perovskite materials, the coupling between their conduction and valence bands is considered to be minimal.[49] The single-band Schrödinger equation can be expressed as:[50]

$$\boldsymbol{H}\Psi_n(\boldsymbol{r}) = E_n\Psi_n(\boldsymbol{r}) \tag{1}$$

$$-\frac{\hbar^2}{2}\nabla\cdot\boldsymbol{M}(\boldsymbol{r})\nabla + \mathrm{V}(\mathbf{r})\Psi_n(\boldsymbol{r}) = E_n\Psi_n(\boldsymbol{r}) \tag{2}$$

with $\mathrm{V}(\mathrm{r})$ being the potential energy, and the effective mass tensor $\boldsymbol{M}(x)$ as:

$$\begin{pmatrix} 1/m_{xx} & 1/m_{xy} & 1/m_{xz} \\ 1/m_{yx} & 1/m_{yy} & 1/m_{yz} \\ 1/m_{zx} & 1/m_{yz} & 1/m_{zz} \end{pmatrix} \tag{3}$$

The 1D single-band effective mass Schrödinger equation is written as:

$$\left(-\frac{\hbar^2}{2m_{xx}} + \mathrm{V}(\mathbf{x})\right)\Psi_n(\boldsymbol{x}) = E_n\Psi_n(\boldsymbol{x}) \tag{4}$$

For semiconductors with periodic potential: $\mathrm{V}(\mathbf{x}) = \mathrm{V}(\mathbf{x}+\mathbf{L})$ in which $\mathbf{L}$ is the length of periods, the eigenfunctions can be expressed as:

$$\Psi_{n\boldsymbol{k}}(\boldsymbol{x}) = u_{n\boldsymbol{k}}(\boldsymbol{x})e^{i\boldsymbol{k}\cdot\boldsymbol{x}} \tag{5}$$

With $u_{n\boldsymbol{k}}(\boldsymbol{x}) = u_{n\boldsymbol{k}}(\boldsymbol{x}+\boldsymbol{L})$. In the multi-band $\boldsymbol{k}\cdot\boldsymbol{p}$ method, the relativistic effect of spin is taken into consideration by adding an additional term $\boldsymbol{H_{so}}$ which has the form of:

$$\boldsymbol{H_{so}} = \frac{\hbar^2}{4m_0^2c^2}(\nabla V \times \boldsymbol{p}) \cdot \sigma \tag{6}$$

in which m_0 is the electron mass, c is the speed of light in vacuum, $\boldsymbol{p}$ is the momentum operator, and σ is the vector of the Pauli matrices. Taken together, the Schrödinger equation can be written as:

$$(\boldsymbol{H_0} + \boldsymbol{H_{so}})\Psi_{n\boldsymbol{k}}(x) = E_n(\boldsymbol{k})\Psi_{n\boldsymbol{k}}(\boldsymbol{x}) \tag{7}$$

After inserting the Bloch function $\Psi_{nk}(x)$ and cancelling $e^{i\boldsymbol{K}\cdot\boldsymbol{x}}$ term, one obtains:

$$\left(\frac{\boldsymbol{p}^2}{2m_0} + V(x) + \frac{\hbar^2k^2}{2m_0} + \frac{\hbar}{m_0}\boldsymbol{k}\cdot\boldsymbol{p} + \frac{\hbar^2}{4m_0^2c^2}(\nabla V \times \boldsymbol{p})\cdot\sigma\right)u_{n\boldsymbol{k}}(\boldsymbol{x}) = E_n(\boldsymbol{k})u_{n\boldsymbol{k}}(\boldsymbol{x}) \tag{8}$$

Electronic structures were represented within both the single-band and eight-band effective mass function approximations with periodic potentials. The wavefunctions, energy levels and band edges along the QW depth were calculated at room temperature in this study. We use eight-band $\boldsymbol{k}\cdot\boldsymbol{p}$ Schrödinger equation to derive the wavefunctions, energy levels and interband transition energies of the QW structures unless otherwise stated. The probability of the ISB transitions between an initial state *i* and a final state *f* can be obtained by evaluating the ISB transition dipole moments $\boldsymbol{z_{fi}}$:[44, 51]

$$\left|\boldsymbol{z_{fi}}\right| \propto \left|\int \psi_f^*(z) \times z \times \psi_i(z)\mathrm{d}z\right| \tag{9}$$

with ψ_f^* and ψ_i being the wavefunctions of the initial and final states, and z the direction perpendicular to the QW layers.

For absorption coefficients in doped structures, Poisson equation was also included to reflect charge self-consistence:[50]

$$\nabla \cdot \left(\varepsilon_0 \varepsilon_r(\boldsymbol{x}) \nabla \phi(\boldsymbol{x})\right) = -\rho(\boldsymbol{x}) \tag{10}$$

where ε_0 is the vacuum permittivity, $\varepsilon_r(\boldsymbol{x})$ is the static dielectric constant tensor at position $\boldsymbol{x}$ and ϕ is the electrostatic potential. Based on the ISB transition dipole matrix element $\boldsymbol{z_{fi}}$, we further calculate the absorption coefficient using:[51, 52]

$$\alpha(\omega) = \frac{e^2 \omega (N_i - N_f)}{\hbar \varepsilon_0 n c} z_{ij}^2 \frac{\Gamma/2}{(E_j - E_i - \hbar\omega)^2 + \Gamma^2/4} \tag{11}$$

where c is the speed of light in vacuum, n is the refractive index, and Γ is the energy linewidth in terms of full-width-half-maximum (FWHM) which is derived as $\Gamma = \hbar/\tau$ with τ being the relaxation time. N_i is the volume carrier density which can be derived from the 2D density of states and Fermi-Dirac function:[44, 51]

$$N_i = \frac{m^* k_B T}{\pi \hbar^2} ln\left(\frac{1}{1 - f_i}\right) = \frac{m^* k_B T}{\pi \hbar^2} \ln\left(1 + \exp\left(\frac{E_f - E_i}{k_B T}\right)\right) \tag{12}$$

where k_B is the Boltzmann constant, T is the temperature and f_i is the occupancy probability of the ith band based on the Fermi-Dirac distribution.

ASSOCIATED CONTENT

Supporting Information:

Intersubband transitions of a thin quantum well with different doping concentrations; absorption coefficients of SQW and DQW; scattering lifetime and optical gain.

AUTHOR INFORMATION

Corresponding Author

Email: xuedan.ma@anl.gov

Notes

The authors declare no competing financial interests.

ACKNOWLEDGMENT

We acknowledge support from the National Science Foundation DMR Program under awards no. DMR-1905990 and CBET Program under award no. 2025214. Use of the Center for Nanoscale Materials, an Office of Science user facility, was supported by the U.S. Department of Energy, Office of Science, Office of Basic Energy Sciences, under Contract No. DE-AC02-06CH11357. We thank Dr. Stefan Birner for assistance in the simulation. This work was performed, in part, at the Center for Integrated Nanotechnologies, an Office of Science User Facility operated for the U.S. Department of Energy (DOE) Office of Science by Los Alamos National Laboratory (Contract 89233218CNA000001) and Sandia National Laboratories (Contract DE-NA-0003525)

REFERENCES

(1) Sassi, S.; Parret, R.; Nanot, S.; Bruna, M.; Borini, S.; De Fazio, D.; Zhao, Z.; Lidorikis, E.; Koppens, F. H. L.; Ferrari, A. C.; et al. Graphene-based mid-infrared room-temperature pyroelectric bolometers with ultrahigh temperature coefficient of resistance. *Nat. Commun.* **2017**, *8*, 14311.
(2) Rogalski, A. Progress in focal plane array technologies. *Prog. Quant. Electron.* **2012**, *36*, 342-373.

(3) Faist, J.; Capasso, F.; Sivco, D. L.; Sirtori, C.; Hutchinson, A. L.; Cho, A. Y. Quantum Cascade Laser. *Science* **1994**, *264*, 553-556.
(4) Yang, R. Q. Infrared laser based on intersubband transitions in quantum wells. *Superlattices Microst.* **1995**, *17*, 77-83.
(5) Khiar, A.; Eibelhuber, M.; Volobuev, V.; Witzan, M.; Hochreiner, A.; Groiss, H.; Springholz, G. Vertical external cavity surface emitting PbTe/CdTe quantum dot lasers for the mid-infrared spectral region. *Opt. Exp.* **2014**, *39*, 6577-6580.
(6) Phillips, J. Evaluation of the fundamental properties of quantum dot infrared detectors. *J. Appl. Phys.* **2002**, *91*, 4590.
(7) Deng, Z.; Jeong, K. S.; Guyot-Sionnest, P. Colloidal Quantum Dots Intraband Photodetectors. *ACS Nano* **2014**, *8*, 11707-11714.
(8) Herz, L. M. Charge-Carrier Mobilities in Metal Halide Perovskites: Fundamental Mechanisms and Limits. *ACS Energy Lett.* **2017**, *2*, 1539-1548.
(9) Kim, J.; Lee, S.-H.; Lee, J. H.; Hong, K.-H. The Role of Intrinsic Defects in Methylammonium Lead Iodide Perovskite. *J. Phys. Chem. Lett.* **2014**, *5*, 1312-1317.
(10) Steirer, K. X.; Schulz, P.; Teeter, G.; Stevanovic, V.; Yang, M.; Zhu, K.; Berry, J. J. Defect Tolerance in Methylammonium Lead Triiodide Perovskite. *ACS Energy Lett.* **2016**, *1*, 360-366.
(11) Stoumpos, C. C.; Malliakas, C. D.; Kanatzidis, M. G. Semiconducting Tin and Lead Iodide Perovskites with Organic Cations: Phase Transitions, High Mobilities, and Near-Infrared Photoluminescent Properties. *Inorg. Chem.* **2013**, *52*, 9019-9038.
(12) Lee, K. J.; Turedi, B.; Sinatra, L.; Zhumekenov, A. A.; Maity, P.; Dursun, I.; Naphade, R.; Merdad, N.; Alsalloum, A.; Oh, S.; et al. Perovskite-Based Artificial Multiple Quantum Wells. *Nano Lett.* **2019**, *19*, 3535-3542.
(13) Erkılıç, U.; Solís-Fernández, P.; Ji, H. G.; Shinokita, K.; Lin, Y.-C.; Maruyama, M.; Suenaga, K.; Okada, S.; Matsuda, K.; Ago, H. Vapor Phase Selective Growth of Two-Dimensional Perovskite/WS2 Heterostructures for Optoelectronic Applications. *ACS Appl. Mater. Interfaces* **2019**, *11*, 40503-40511.
(14) Dou, L.; Wong, A. B.; Yu, Y.; Lai, M.; Kornienko, N.; Eaton, S. W.; Fu, A.; Bischak, C. G.; Ma, J.; Ding, T.; et al. Atomically thin two-dimensional organic-inorganic hybrid perovskites. *Science* **2015**, *349*, 1518-1521.
(15) Wang, Q.; Shao, Y.; Xie, H.; Lyu, L.; Liu, X.; Gao, Y.; Huang, J. Qualifying composition dependent *p* and *n* self-doping in $CH_3NH_3PbI_3$. *Appl. Phys. Lett.* **2014**, *105*, 163508.
(16) Milot, R. L.; Klug, M. T.; Davies, C. L.; Wang, Z.; Kraus, H.; Snaith, H. J.; Johnston, M. B.; Herz, L. M. The Effects of Doping Density and Temperature on the Optoelectronic Properties of Formamidinium Tin Triiodide Thin Films. *Adv. Mater.* **2018**, *30*, 1804506.
(17) Yu, Y.; Zhang, D.; Kisielowski, C.; Dou, L.; Kornienko, N.; Bekenstein, Y.; Wong, A. B.; Alivisatos, A. P.; Yang, P. Atomic Resolution Imaging of Halide Perovskites. *Nano Lett.* **2016**, *16*, 7530-7535. DOI: doi.org/10.1021/acs.nanolett.6b03331.
(18) Whitcher, T. J.; Gomes, L. C.; Zhao, D.; Bosman, M.; Chi, X.; Wang, Y.; Carvalho, A.; Hui, H. K.; Chang, Q.; Breese, M. B. H.; et al. Dual phases of crystalline and electronic structures in the nanocrystalline perovskite CsPbBr3. *NPG Asia Mater.* **2019**, *11*, 70. DOI: doi.org/10.1038/s41427-019-0170-6.
(19) Becker, M.; Vaxenburg, R.; Nedelcu, G.; Sercel, P. C.; Shabaev, A.; Mehl, M. J.; Michopoulos, J. G.; Lambrakos, S. G.; Bernstein, N.; Lyons, J. L.; et al. Bright triplet excitons in caesium lead halide perovskites. *Nature* **2018**, *553*, 189-193.

(20) Ompong, D.; Inkoom, G.; Singh, J. Effective mass of heavy, light, and spin split-off band electron and hole g-factor in cubic perovskite materials. *J. Appl. Phys.* **2020**, *128*, 235109.
(21) Ashari-Astani, N.; Meloni, S.; Salavati, A. H.; Palermo, G.; Grätzel, M.; Rothlisberger, U. Computational Characterization of the Dependence of Halide Perovskite Effective Masses on Chemical Composition and Structure. *J. Phys. Chem. C* **2017**, *121*, 23886-23895.
(22) He, Y.; Matei, L. l.; Jung, H. J.; McCall, K. M.; Chen, M.; Stoumpos, C. C.; Liu, Z.; Peters, J. A.; Chung, D. Y.; Wessels, B. W.; et al. High spectral resolution of gamma-rays at room temperature by perovskite CsPbBr3 single crystals. *Nat. Commun.* **2018**, *9*, 1609.
(23) Zhang, B.; Wang, F.; Zhang, H.; Xiao, B.; Sun, Q.; Guo, J.; Hafsia, A. B.; Shao, A.; Xu, Y.; Zhou, J. Defect proliferation in CsPbBr3 crystal induced by ion migration. *Appl. Phys. Lett.* **2020**, *116*, 063505.
(24) Ahmad, M.; Rehman, G.; Ali, L.; Shafiq, M.; Iqbal, R.; Ahmad, R.; Khan, T.; Jalali-Asadabadi, S.; Maqbool, M.; Ahmad, I. Structural, electronic and optical properties of CsPbX3(X=Cl, Br, I) for energy storage and hybrid solar cell applications. *J. Alloys Compd.* **2017**, *705*, 828-839.
(25) Ghaithan, H. M.; Alahmed, Z. A.; Qaid, S. M. H.; Hezam, M.; Aldwayyan, A. S. Density Functional Study of Cubic, Tetragonal, and Orthorhombic CsPbBr3 Perovskite. *ACS Omega* **2020**, *5*, 7468-7480.
(26) Puppin, M.; Polishchuk, S.; Colonna, N.; Crepaldi, A.; Dirin, D. N.; Nazarenko, O.; De Gennaro, R.; Gatti, G.; Roth, S.; Barillot, T.; et al. Evidence of Large Polarons in Photoemission Band Mapping of the Perovskite Semiconductor CsPbBr3. *Phys. Rev. Lett.* **2020**, *124*, 206402.
(27) Yettapu, G. R.; Talukdar, D.; Sarkar, S.; Swarnkar, A.; Nag, A.; Ghosh, P.; Mandal, P. Terahertz Conductivity within Colloidal CsPbBr3 Perovskite Nanocrystals: Remarkably High Carrier Mobilities and Large Diffusion Lengths. *Nano Lett.* **2016**, *16*, 4838-4848.
(28) Protesescu, L.; Yakunin, S.; Bodnarchuk, M. I.; Krieg, F.; Caputo, R.; Hendon, C. H.; Yang, R.; Walsh, A.; Kovalenko, M. V. Nanocrystals of Cesium Lead Halide Perovskites (CsPbX3, X = Cl, Br, and I): Novel Optoelectronic Materials Showing Bright Emission with Wide Color Gamut. *Nano Lett.* **2015**, *15*, 3692-3696.
(29) Saran, R.; Heuer-Jungemann, A.; Kanaras, A. G.; Curry, R. J. Giant Bandgap Renormalization and Exciton–Phonon Scattering in Perovskite Nanocrystals. *Adv. Opt. Mater.* **2017**, *5*, 1700231.
(30) Zhou X.; Zhang, Z. Electron–phonon coupling in CsPbBr3. *AIP Adv.* **2020**, *10*, 125015.
(31) Lohmann, S. K.; Cai, T.; Morrow, D. J.; Chen, O.; Ma, X. Brightening of Dark States in CsPbBr3 Quantum Dots Caused by Light-Induced Magnetism. *Small* **2021**, *17*, 2101527. DOI: doi.org/10.1002/smll.202101527.
(32) Ha, S.; Su, R.; Xing, J.; Zhang, Q.; Xiong, Q. Metal halide perovskite nanomaterials: synthesis and applications. *Chem. Sci.* **2017**, *8*, 2522-2536.
(33) He, Y.; Stoumpos, C. C.; Hadar, I.; Luo, Z.; McCall, K. M.; Liu, Z.; Chung, D. Y.; Wessels, B. W.; Kanatzidis, M. G. Demonstration of Energy-Resolved γ-Ray Detection at Room Temperature by the CsPbCl3 Perovskite Semiconductor. *J. Am. Chem. Soc.* **2021**, *143*, 2068-2077.
(34) Ji, W.; Tian, Y.; Zeng, Q.; Qu, S.; Zhang, L.; Jing, P.; Wang, J.; Zhao, J. Efficient Quantum Dot Light-Emitting Diodes by Controlling the Carrier Accumulation and Exciton Formation. *ACS Appl. Mater. Interfaces* **2014**, *6*, 14001-14007.
(35) People, R.; Bean, J. C. Calculation of critical layer thickness versus lattice mismatch for Ge_xSi_{1-x}/Si strained-layer heterostructures. *Appl. Phys. Lett.* **1985**, *47*, 322.
(36) Islam, M. N.; Hadi, M. A.; Podder, J. Influence of Ni doping in a lead-halide and a lead-free halide perovskites for optoelectronic applications. *AIP Adv.* **2019**, *9*, 125321.

(37) Ravi, V. K.; Markad, G. B.; Nag, A. Band Edge Energies and Excitonic Transition Probabilities of Colloidal CsPbX3 (X = Cl, Br, I) Perovskite Nanocrystals. *ACS Energy Lett.* **2016**, *1*, 665-671.
(38) Hu, Y.; Wang, Q.; Shi, Y.; Li, M.; Zhang, L.; Wang, Z.; Liao, L. Vacuum-evaporated all-inorganic cesium lead bromine perovskites for high-performance light-emitting diodes. *J. Mater. Chem. C* **2017**, *5*, 8144-8149.
(39) Gauthier-Lafaye, O.; Boucaud, P.; Julien, F. H.; Sauvage, S.; Cabaret, S.; Lourtioz, J.-M.; Thierry-Mieg, V.; Planel, R. Long-wavelength (≈15.5 μm) unipolar semiconductor laser in GaAs quantum wells. *Appl. Phys. Lett.* **1997**, *71*, 3619.
(40) Tao, S.; Schmidt, I.; Brocks, G.; Jiang, J.; Tranca, I.; Meerholz, K.; Olthof, S. Absolute energy level positions in tin- and lead-based halide perovskites. *Nat. Commun.* **2019**, *10*, 2560. DOI: DOI: 10.1038/s41467-019-10468-7.
(41) Fu, H.; Chen, H.; Huang, X.; Lu, Z.; Zhao, Y. Theoretical analysis of modulation doping effects on intersubband transition properties of semipolar AlGaN/GaN quantum well. *J. Appl. Phys.* **2017**, *121*, 014501. DOI: doi.org/10.1063/1.4972975.
(42) Euvrard, J.; Yan, Y.; Mitzi, D. B. Electrical doping in halide perovskites. *Nat. Rev. Mater.* **2021**, *6*, 531-549.
(43) Mulder, J. T.; du Fossé, I.; Jazi, M. A.; Manna, L.; Houtepen, A. J. Electrochemical p-Doping of CsPbBr3 Perovskite Nanocrystals. *ACS Energy Lett.* **2021**, *6*, 2519-2525.
(44) Lyman, J. E.; Krishnamoorthy, S. Theoretical investigation of optical intersubband transitions and infrared photodetection in β-(Al_xGa_{1-x})2O3/Ga2O3 quantum well structures. *J. Appl. Phys.* **2020**, *127*, 173102.
(45) Billaha, A.; Das, M. K. Influence of doping on the performance of GaAs/AlGaAs QWIP for long wavelength applications. *Opto−Electron. Rev.* **2016**, *24*, 25–33. DOI: doi.org/10.1515/oere-2016-0006.
(46) Ramade, J.; Andriambariarijaona, L. M. S., V.; ; Goubet, N.; Legrand, L.; Barisien, T.; Bernardot, F.; Testelin, C.; Lhuillier, E.; Bramati, A.; Chamarro, A. Exciton-phonon coupling in a CsPbBr3 single nanocrystal. *Appl. Phys. Lett.* **2018**, *112*, 072104. DOI: doi.org/10.1063/1.5018413.
(47) Tomić, S.; Tadić, M.; Milanović, V.; Ikonić, Z. The optimization of optical gain in the intersubband quantum well laser. *J. Appl. Phys.* **2000**, *87*, 7965.
(48) Birner, S.; Hackenbuchner, S.; Sabathil, M.; Zandler, G.; Majewski, J. A.; Andlauer, T.; Zibold, T.; Morschl, R.; Trellakis, A.; Vogl, P. Modeling of Semiconductor Nanostructures with nextnano^3. *Acta Phys. Pol. A* **2006**, *110*, 111-124.
(49) Zhao, H.; Arif, R. A.; Ee, Y.-K.; Tansu, N. Self-Consistent Analysis of Strain-Compensated InGaN–AlGaN Quantum Wells for Lasers and Light-Emitting Diodes. *IEEE J. Quantum Electron.* **2009**, *45*, 66 - 78.
(50) Birner, S. Modeling of semiconductor nanostructures and semiconductor–electrolyte interfaces. Technischen Universität München, MÜNCHEN, 2011.
(51) Cheninia, L.; Aissat, A.; Vilcot, J. P. Optimization of inter-subband absorption of InGaAsSb/GaAs quantum wells structure. *Superlattice Miscrost.* **2019**, *129*, 115-123.
(52) Fasit, J. *Quantum Cascade Lasers*; Oxford Press, 2013.